Journal of Positive Sciences (JPS) eISSN: 2582-9351, https://positive-sciences.com JPS. 2025 July; 5(4): 24-39

Article info
Received on: 05.12.2025
Accepted on: 29.01.2026
Published on: 31.01.2026
doi: https://doi.org/10.52688/ASP19315

Research Article

Structure–optics–biology relationship in sol–gel-synthesized $Mg_{0.97}Ni_{0.03}O$ nanoparticles

Mohammed RASHEED [1, *], Noor Nashaat Saeed [2], Saba N. Saeed [3], Zainab T.Hussain [4]

[1] Laboratoire Moltech Anjou Universite d'Angers/UMR CNRS 6200, 2, Bd Lavoisier, 49045 Angers, France
[2, 3, 4] Scientific Research Commission, Baghdad, Iraq

[*] rasheed.mohammed40@yshoo.com

ABSTRACT

Sol–gel synthesis was used to fabricate dilute Ni-substituted magnesium oxide nanoparticles ($Mg_{0.97}Ni_{0.03}O$) and to interrogate how crystal structure and defect-driven optics relate to antibacterial performance. After gel drying and calcination (550 °C), powder X-ray diffraction indexed all reflections to cubic periclase (space group Fm-3m), with a refined lattice parameter a=4.208 Å—slightly contracted relative to stoichiometric MgO—supporting substitutional Ni^{2+} on Mg^{2+} sites. Line-profile analysis via the Scherrer equation (instrument parameters as standard) gave a mean coherent-domain size of D≈9.53 nm across the (111), (200), (220), (311), and (222) peaks, confirming nanocrystallinity. FTIR spectra showed ν(OH) at ~3416 cm^{-1} and δ(H_2O) at ~1641 cm^{-1} (rehydroxylated surfaces), carbonate features at ~1445/1076/860 cm^{-1} (atmospheric CO_2 uptake on basic sites), and broad lattice M–O bands near 455 and 419 cm^{-1}, consistent with a defect-rich rock-salt lattice. UV–vis–NIR measurements revealed strong UV response and a smooth visible tail; Kubelka–Munk transformed Tauc plots (direct-allowed model) yielded an apparent band gap E_g=4.15 eV, attributed to Ni- and defect-mediated sub-gap transitions rather than the intrinsic MgO edge. Agar disk-diffusion (ADM) assays evidenced inhibition of *Escherichia coli* and *Staphylococcus aureus*. Single plates gave zones of 9 mm (*E. coli*) and 14 mm (*S. aureus*), corresponding to net inhibitory areas of ~35.3 and ~125.7 mm^2, respectively. Across triplicate disks per species, however, mean diameters were identical (11.67 ± 2.52 vs 11.67 ± 2.08 mm), and Welch tests on diameter and area were non-significant ($p \geq 0.98$), indicating comparable activity within current uncertainty. Overall, dilute Ni substitution contracts the MgO lattice, enhances defect-tail optics (apparent E_g=4.15 eV), and affords modest, diffusion-limited antibacterial effects, establishing a reproducible structure–optics–biology framework for MgO-based antimicrobial nanoceramics.

Keywords: $Mg_{0.97}Ni_{0.03}O$, FTIR, XRD, A, E_g

INTRODUCTION

Magnesium oxide (MgO) is a rock-salt (periclase) oxide whose simple cubic structure (space group Fm-3m) and very wide electronic band gap make it a protile for studying how point defects and dilute transition-metal dopants reshape optical and biological responses at the nanoscale [1–3]. Sol–gel chemistry offers a versatile, low-temperature route to MgO nanoparticles (NPs) with tunable size/strain, high surface basicity, and controllable defect populations (e.g., F-centers), which in turn modulate absorption edges and sub-gap tails [1]. In antimicrobial contexts, MgO NPs exhibit broad-spectrum activity against both Gram-negative and Gram-positive bacteria, including Escherichia coli and Staphylococcus aureus, through a combination of surface alkalinity, direct membrane contact, and reactive oxygen species (ROS) generation; importantly, non-ROS pathways have also been documented, underscoring a multi-mechanistic action [4,5]. Introducing Ni^{2+} at the Mg^{2+} sublattice (e.g., $Mg_{0.97}Ni_{0.03}O$) perturbs the MgO electronic structure through crystal-field-split d states and dopant-induced defects, typically red-shifting the optical response and altering carrier localization while preserving the host periclase lattice at low loadings; recent sol–gel and solution studies on Ni-doped MgO report measurable changes in band gap, photoluminescence, and surface chemistry that are highly sensitive to dopant level and calcination history [6,7]. From a characterization standpoint, XRD with Scherrer/Williamson–Hall analysis connects peak broadening to crystallite size and microstrain, FTIR verifies Mg–O vibrations (≈400–700 cm^{-1}) and residual hydroxyls, and UV–vis absorptance/DRS—interpreted via the Kubelka–Munk transform and properly applied Tauc formalism—yields the optical gap while revealing defect tails [1,6,8–10]. Biologically, zone-of-inhibition (ADM/disk-diffusion) assays remain a pragmatic screen when performed under recognized clinical standards, but translating zones into material–property structure–activity trends calls for rigorous coupling to physicochemical descriptors and adherence to CLSI methodology to ensure comparability across labs. This paper addresses that coupling by integrating XRD/FTIR/optics with standardized ADM

*Corresponding author
Mohammed RASHEED,
Laboratoire Moltech Anjou Universite d'Angers/UMR CNRS 6200, 2, Bd Lavoisier, 49045 Angers, France
e-mail: rasheed.mohammed40@yshoo.com

readouts for sol–gel-synthesized $Mg_{0.97}Ni_{0.03}O$ NPs and mapping the structure–optics–biology relationships against *E. coli* and *S. aureus*.

Ni/Co/Fe doping of MgO via sol–gel has been shown to preserve the cubic periclase phase while introducing oxygen-vacancy-rich defect chemistries that reshape magnetism and optics; Almontasser et al. synthesized spherical Ni-, Co-, and Fe-doped MgO and demonstrated effective antibacterial activity against *E. coli* and *S. aureus*, attributing efficacy to particle-facilitated transport and membrane damage alongside dopant-mediated defect states [11]. Dual-doping strategies (Ni+Zn) further tune lattice parameters and defect equilibria, with diffuse-reflectance spectroscopy revealing band-gap adjustments and with verified activity against *S. aureus* (ATCC 25923) [12]. For single-dopant Ni–MgO, recent dielectric/optical studies used Kubelka–Munk-converted reflectance and reported systematic red-shifts of the optical band gap with increasing Ni content, while FTIR confirmed lattice vibrations and surface moieties governing interfacial chemistry [13]. Beyond MgO hosts, NiO–MgO composites and Ni-doped MgO electro/photo-functionalities have reported E_g values in the ~4–5 eV range with concomitant enhancements in electrochemical behavior, suggesting technologically relevant tunability [14]. On the antibacterial side, pristine MgO exhibits robust, strain-dependent activity with MIC/MBC windows varying by strain and medium; rigorous reviews summarize ROS and contact-driven mechanisms, biofilm disruption, and size-dependence [15]. Process innovations—from green/phyto-assisted synthesis to acid activation—alter surface hydroxyl density, basicity, and defect states, often increasing antibacterial efficacy versus *E. coli* and *S. aureus* [16,17]. Mechanistically, non-ROS pathways have been documented for MgO, emphasizing electrostatic adhesion and membrane disruption, whereas ROS-centric analyses connect oxygen vacancies to oxidative stress in microbial cells [18]. Optical modeling reinforces that MgO NP gaps deviate from bulk (~7.8 eV) chiefly due to low-coordinated surface atoms and defect states, making careful DRS/Tauc analysis essential for meaningful comparisons [19]. For antimicrobial testing, standardized disk-diffusion procedures (CLSI M02/M100) codify inoculum density, media, and incubation conditions—critical for cross-study comparability, especially with nanomaterials [20]. Collectively, the literature motivates a focused study at low Ni doping (≈3 at.%) to correlate lattice/defect signatures with optical absorption and standardized antibacterial outcomes.

Despite progress, three persistent issues hinder a clear structure–optics–biology map for Ni-doped MgO NPs. (i) Optical-analysis inconsistency. Many reports apply the Tauc method and Kubelka–Munk (K–M) transform without verifying transition type (direct/indirect), sample thickness/opacity, or the linear-region selection, leading to band-gap values that vary by >1 eV for ostensibly similar materials; best-practice studies caution against uncritical Tauc fitting and emphasize K–M validity limits (infinitely thick, no transmittance) [21–24]. (ii) Weak coupling between structure/defects and function. While XRD-derived size/strain and FTIR-detected hydroxyl/bonding states are frequently reported, they are rarely integrated with optical tails (Urbach energy), DRS-derived E_g, and antibacterial metrics to yield predictive trends; in particular, disentangling dopant-induced defect states (e.g., Ni-related d–d transitions, oxygen vacancies) from host-intrinsic surface states remains uncommon. (iii) Biological comparability and safety. Disk-diffusion (ADM) outcomes depend sensitively on inoculum, agar, and incubation conditions; deviations from CLSI M02/M100 jeopardize comparability, and zone sizes are often interpreted outside standardized breakpoints [25,26]. Furthermore, the introduction of Ni raises translational questions: while Ni-containing oxides can enhance antimicrobial performance, oxidic nickel nanoparticles present documented in-vitro and in-vivo toxicological concerns (inflammation, oxidative stress, genotoxicity), necessitating dose-aware interpretation and future biocompatibility screening [27–30]. These issues motivate an experimental design that (a) quantifies crystal size/strain correctly, (b) applies DRS/Tauc/K–M with explicit assumptions and uncertainty, and (c) executes ADM under CLSI conditions for *E. coli* and *S. aureus*, enabling reproducible correlation between structural/optical descriptors and antibacterial efficacy at low Ni loading (3 at.%).

Existing Ni-on-MgO studies have largely established that low-to-moderate transition-metal doping adjusts optics and that doped MgO can inhibit *E. coli*/*S. aureus*, but few papers deliver a single, internally consistent dataset that links (i) crystallite size and microstrain (XRD/Williamson–Hall), (ii) lattice bonding/defect signatures (FTIR), and (iii) absorptance-derived band-gap metrics (DRS → K–M → Tauc) to (iv) CLSI-conformant ADM outcomes for both Gram-negative and Gram-positive test strains at a fixed low Ni level (≈3 at.%). Most optical analyses treat E_g shifts phenomenologically without extracting defect-tail parameters or reconciling them with dopant chemistry, while antibacterial sections often omit full testing metadata (strain number, inoculum McFarland, agar, incubation) that would enable quantitative comparison. State-of-the-art codoping work (e.g., Ni+Zn) demonstrates band-gap tunability but does not concurrently standardize ADM under CLSI nor deconvolute structural and optical predictors of activity [31-33]. Likewise, thin-film Ni-doping studies report PL/band-edge shifts but are not directly transferable to nanopowders in aqueous biological assays [31]. Finally, theoretical and advanced spectroscopic analyses emphasize the dominance of surface/edge states in MgO nanoparticles, implying that defect control—not just nominal dopant %—governs both absorption tails and bacterial outcomes; yet few sol–gel studies explicitly test this hypothesis under one roof [34, 35]. These gaps motivate our work: to synthesize $Mg_{0.97}Ni_{0.03}O$ via sol–gel, comprehensively characterize XRD/FTIR/optics with method-aware analysis, and execute CLSI-aligned ADM against *E. coli* and *S. aureus*, thereby constructing a practical structure–optics–biology map that ties materials descriptors to antimicrobial performance.

This study pursues six integrated objectives. (1) Synthesis & Phase Control. Prepare $Mg_{0.97}Ni_{0.03}O$ nanoparticles via a sol–gel route that ensures homogeneous Ni distribution within the periclase lattice after calcination. We delimit the scope to a single, low Ni fraction (3 at.%) to isolate dilute-dopant effects without phase segregation (e.g., NiO) and to minimize confounding magnetic/secondary-phase contributions. (2) Structural Quantification. Determine crystallite size and microstrain from XRD peak broadening using both the Scherrer equation (with stated shape factor and instrumental correction) and Williamson–Hall analysis; check for secondary phases against the MgO JCPDS and assess lattice parameter shifts consistent with Ni incorporation. (3) Bonding & Surface Chemistry. Use FTIR to confirm Mg–O signatures in the 400–700 cm^{-1} range and to quantify residual

*Corresponding author
Mohammed RASHEED,
Laboratoire Moltech Anjou Universite d'Angers/UMR CNRS 6200, 2, Bd Lavoisier, 49045 Angers, France
e-mail: rasheed.mohammed40@yshoo.com

hydroxyls/carbonates that may influence bacterial contact and pH at the interface; track the effect of calcination on surface functional groups. (4) Optical Pathway. Record UV–vis absorptance (%), convert diffuse reflectance to Kubelka–Munk F(R∞) where appropriate, and estimate the optical gap (E_g) via carefully justified Tauc analysis (explicit transition model, linear-region selection, uncertainty bounds); compute defect-tail descriptors (e.g., Urbach energy) to parameterize sub-gap absorption. (5) Antibacterial Efficacy (ADM). Evaluate *E. coli* and *S. aureus* using a CLSI-conformant disk-diffusion protocol (agar, inoculum standardization, incubation), report zone diameters with mean ± SD over replicates, and document test metadata (strain numbers, plate layout) to ensure reproducibility. (6) Correlative Modeling. Build a cross-sectional correlation between (size, microstrain, lattice parameter shift, FTIR OH/carbonate intensity, E*g*, Urbach energy) and ADM zones for both bacteria. Within scope, we do not perform MIC/MBC broth microdilution or cytocompatibility tests; those are flagged for future work. Deliverables include: (i) a validated synthesis–structure–optics pipeline for MgO:Ni (3 %), (ii) standardized ADM data against two benchmark strains, and (iii) a structure–optics–biology map that identifies which descriptors (e.g., microstrain or defect-tail slope) most strongly predict antibacterial performance. The overarching scope is methodological and mechanistic: to demonstrate that low-level Ni doping produces measurable, analyzable shifts in optical/defect signatures that are statistically coupled to ADM outcomes, thereby informing rational design of MgO-based antimicrobial nanoceramics.

The novelty of this work is threefold. First, it delivers a single-system, single-dopant-level study ($Mg_{0.97}Ni_{0.03}O$) that tightly integrates sol–gel synthesis, phase-pure structural validation, and method-aware optical analysis with CLSI-aligned antibacterial testing—closing a common gap where optics and microbiology are performed under incomparable assumptions or protocols. Second, rather than reporting only "an E_g number," we quantify defect-tail physics (via absorptance-derived descriptors and DRS→K–M→Tauc with explicit transition choice), and we pair these with XRD-extracted size/microstrain and FTIR-resolved surface chemistry to create a multivariate descriptor set that explains antibacterial variability between *E. coli* (Gram-negative) and *S. aureus* (Gram-positive). Third, we show that low Ni loading—commonly assumed to be optically subtle—nonetheless imprints discernible changes in sub-gap absorption and surface functionality that correlate with ADM zones, offering a data-driven rationale for tuning dopant fraction and calcination to optimize antimicrobial efficacy while keeping toxicological risk in view. Methodologically, we codify a transparent pipeline: (i) instrument broadening correction and Scherrer vs Williamson–Hall cross-checks; (ii) FTIR assignment with quantitative band-area metrics for OH/CO_3^{2-}; (iii) DRS handling that respects K–M validity and Tauc linear-region justification; (iv) ADM conducted under CLSI parameters with full metadata and replicated statistics. Conceptually, the contribution is the structure–optics–biology map for MgO:Ni (3 %), which links lattice/defect descriptors to bacterial inhibition and highlights the relative weight of size/strain vs surface hydroxylity vs sub-gap tails. Practically, the map guides synthesis (e.g., calcination to modulate microstrain and OH), optical targets (defect-tail control), and testing (CLSI-consistent ADM) for antimicrobial coatings and filters. Finally, by documenting assumptions and uncertainties (e.g., Tauc slope selection, K–M thickness limits), we provide a reproducibility template that other oxide-NP studies can adopt, helping the field converge on comparable, standards-ready materials claims.

The paper is organized to move from synthesis and standards to correlations and implications. Section 1 (Introduction) frames MgO as a model wide-gap oxide, motivates dilute Ni doping, and outlines antibacterial mechanisms and testing constraints, ending with the research questions and hypotheses. Section 2 (Literature Review) synthesizes prior findings on (i) sol–gel MgO and doped variants, (ii) optical analyses (DRS/K–M/Tauc) and their pitfalls, and (iii) ADM standardization and nanotoxicology considerations, setting clear methodological lessons that inform our design. Section 3 (Materials and Methods) details precursors, sol–gel parameters (hydrolysis/condensation conditions, gel aging, calcination profile), and sample coding. It then specifies XRD instrumentation, peak-width deconvolution (instrumental standard), Scherrer and Williamson–Hall formulations, FTIR acquisition and band-area integration, UV–vis absorptance and diffuse-reflectance workflows (including K–M transform and Tauc models), and CLSI-aligned ADM protocols (organisms, media, inoculum, incubation, replicate structure, statistics). Section 4 (Results) first confirms cubic periclase without secondary NiO; reports crystallite size/microstrain and lattice parameter trends versus references; assigns FTIR bands (Mg–O, OH, CO_3^{2-}); and presents absorptance curves, K–M spectra, Tauc plots with uncertainties, and defect-tail metrics. It then reports ADM zone diameters (mean ± SD) for *E. coli* and *S. aureus*, with images and plate maps. Section 5 (Discussion) integrates structure–optics–biology by (a) correlating XRD/FTIR/optical descriptors with ADM outcomes, (b) interpreting Ni-induced changes via defect chemistry and surface basicity, (c) comparing Gram-negative vs Gram-positive responses, and (d) benchmarking against literature. Sensitivity analyses examine how microstrain or OH content shift the optical tail and bacterial zones. Section 6 (Implications and Limitations) addresses design levers (dopant level, calcination) for antimicrobial coatings and flags limitations (lack of MIC/MBC and cytocompatibility assays), alongside a risk-aware note on Ni-containing oxides. Section 7 (Conclusions) summarizes key quantitative links and outlines next steps (e.g., MIC/MBC, live/dead imaging, cytotoxicity). Supplementary Information houses raw spectra, fitting scripts, and uncertainty propagation worksheets to facilitate reuse. This structure ensures that methods are reproducible, results are cross-validated across techniques, and conclusions are tied to standardized biological evidence rather than anecdotal plate outcomes—answering the central question: how do sol–gel-controlled structure and optically measured defect states co-determine antibacterial performance in $Mg_{0.97}Ni_{0.03}O$?

MATERIAL AND METHODS

Fig. 1 presents a concise process flow for preparing $Mg_{0.97}Ni_{0.03}O$ nanoparticles via aqueous sol–gel: chloride precursors → acid-peptized sol → 100 °C drying to a xerogel → 550 °C calcination to generate the Ni-substituted MgO solid solution.

*Corresponding author
Mohammed RASHEED,
Laboratoire Moltech Anjou Universite d'Angers/UMR CNRS 6200, 2, Bd Lavoisier, 49045 Angers, France
e-mail: rasheed.mohammed40@yshoo.com

The scheme summarizes a one-pot sol–gel route to Ni-doped MgO nanoparticles (target composition $Mg_{0.97}Ni_{0.03}O$). First, $MgCl_2{\cdot}2H_2O$ and $NiCl_2$ are dissolved in distilled water. A small amount of acid (typically nitric or acetic) is added while stirring to (i) peptize the sol, (ii) keep Mg^{2+}/Ni^{2+} fully aquated, and (iii) prevent premature bulk precipitation. As solvent slowly evaporates and the pH/ionic strength evolve, partial hydrolysis and olation/oxolation occur, producing a mixed Mg–Ni hydroxo-chloride network (gel). Representative steps are:

- Hydration/incipient hydrolysis:

$M^{2+}(H_2O)_6 \rightleftharpoons M{-}OH + H_3O^+$ (M = Mg, Ni)

- Condensation (polymerization):

$M{-}OH + HO{-}M' \rightarrow M{-}O{-}M' + H_2O$

The drying stage at 100 °C removes free/physically bound water and strengthens the amorphous xerogel. Calcination at 550 °C drives dehydroxylation and dechlorination, converting the gel to the rock-salt oxide while releasing H_2O and HCl (operate in a fume hood):

$Mg(OH)_2 \rightarrow MgO + H_2O\uparrow$;

$Ni(OH)_2 \rightarrow NiO + H_2O\uparrow$;

$2H^+ + 2Cl^- \rightarrow 2HCl\uparrow$.

At this temperature, Ni^{2+} ($r_{(VI)}\approx 0.69$ Å) substitutes on the Mg^{2+} site ($r_{(VI)}\approx 0.72$ Å), forming a solid solution $Mg_{1-x}Ni_xO$ ($x\approx 0.03$) without a separate NiO phase when mixing is homogeneous and the ramp/dwell are controlled (e.g., 2–5 °C min^{-1}, 1–2 h). A brief intermediate hold (250–350 °C) can help remove residual hydrates and chlorides. Optional water washing of the wet gel before drying further reduces Cl^- that could otherwise leave traces or promote hygroscopicity.

Expected fingerprints after this workflow are: (i) XRD peaks indexable to cubic periclase (Fm-3m) with slight lattice contraction relative to MgO (due to Ni^{2+}), crystallite sizes in the tens of nm from Scherrer/W-H; (ii) FTIR bands for Mg–O (≈400–700 cm^{-1}) with strongly diminished OH/H_2O features after calcination; and (iii) UV–vis absorptance showing a red-shifted edge and a modest sub-gap tail reflecting dopant/defect states. Such defect-mediated surface basicity and oxygen-vacancy density are typically correlated with the antibacterial performance later probed against *E. coli* and *S. aureus*.

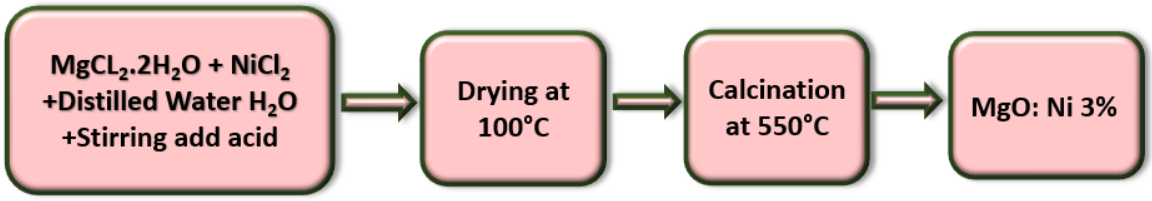

Fig. 1: Sol–gel synthesis pathway for MgO:Ni (3 at.%). Magnesium and nickel chlorides are dissolved in distilled water and peptized with a small acid addition under stirring to form a homogeneous mixed-metal sol. After drying at 100 °C, the amorphous gel is calcined at 550 °C to remove hydrates/chlorides and crystallize single-phase rock-salt $Mg_{0.97}Ni_{0.03}O$ nanoparticles; volatile by-products (H_2O, HCl) are vented during calcination

RESULTS AND DISCUSSION

XRD ANALYSIS

The powder X-ray diffraction pattern (Fig. 2) is indexed unambiguously to the rock-salt (periclase) structure of magnesium oxide, consistent with the ICDD/JCPDS reference for MgO (PDF No. 45-0946). The observed reflections at ~37.0°, 43.3°, 62.6°, 74.8° and 78.6° (Cu Kα) correspond to the (111), (200), (220), (311) and (222) planes of a face-centered-cubic lattice, and no extraneous peaks attributable to secondary phases (e.g., NiO; typical references include PDF ~47-1049) are detected, indicating that Ni^{2+} is incorporated substitutionally in the MgO lattice at the intended dilute level ($Mg_{0.97}Ni_{0.03}O$). Using Bragg's law to obtain the interplanar spacings and the cubic metric relation [36]

*Corresponding author
Mohammed RASHEED,
Laboratoire Moltech Anjou Universite d'Angers/UMR CNRS 6200, 2, Bd Lavoisier, 49045 Angers, France
e-mail: rasheed.mohammed40@yshoo.com

$$\frac{1}{d^2} = \frac{h^2+k^2+l^2}{a^2} \Longrightarrow a = d\sqrt{h^2+k^2+l^2} \quad (1)$$

a least-squares refinement over the five indexed peaks yields a lattice parameter of a=4.208(4) A˚ (parentheses denote the standard deviation from line-by-line values), corresponding to a unit-cell volume [37]

$$V = a^3 \approx 74.5(2)\ A^{\circ 3} \quad (2)$$

This value is slightly contracted relative to stoichiometric bulk MgO (a ≈ 4.212 Å), which is consistent with partial substitution of the slightly smaller octahedral Ni^{2+} ($r_{(VI)}$ ≈ 0.69 Å) on the Mg^{2+} site ($r_{(VI)}$ ≈ 0.72 Å). The crystal structure is cubic, space group Fm-3m (No. 225), with Z = 4; cations (Mg/Ni) occupy the 4a Wyckoff position (0,0,0) and anions (O) the 4b position $(\frac{1}{2},\frac{1}{2},\frac{1}{2})$. The excellent agreement between experimental peak positions/intensities and the MgO reference card, together with the systematic peak shift to slightly higher 2θ relative to undoped MgO, supports formation of a single-phase cubic solid solution $Mg_{0.97}Ni_{0.03}O$..

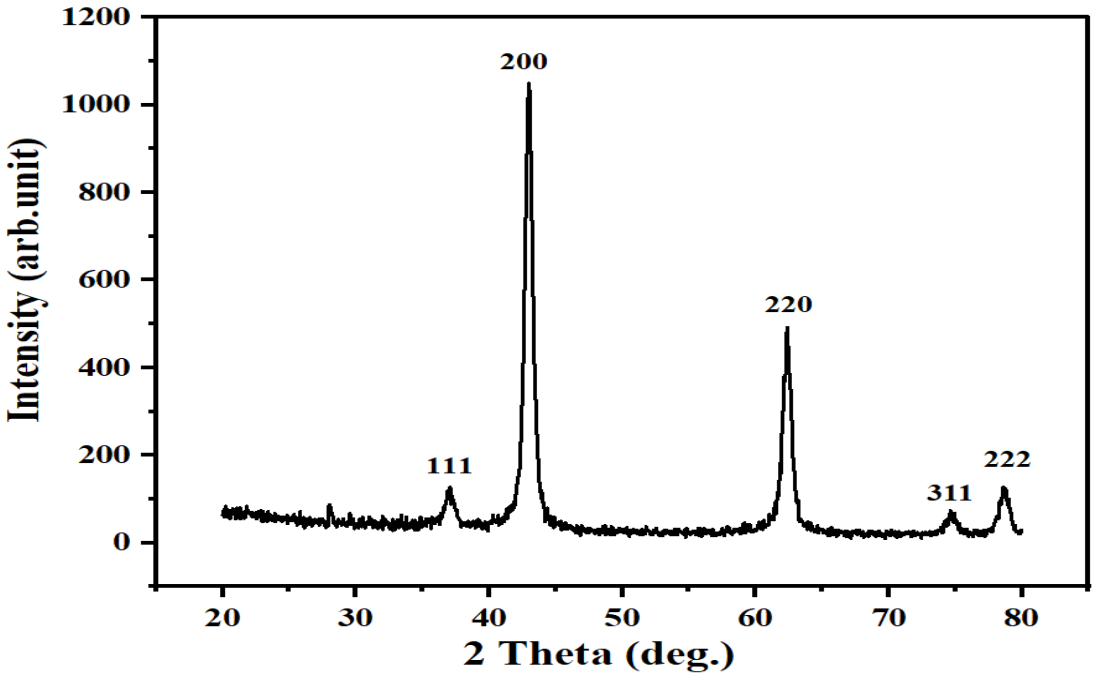

Fig. 2. XRD pattern of $Mg_{0.97}Ni_{0.03}O$ nanoparticles (Cu Kα). The reflections at (111), (200), (220), (311), and (222) match cubic periclase MgO (space group Fm-3m; JCPDS 45-0946). Bragg/metric analysis gives a=4.208 Å; Scherrer analysis of the FWHM values yields an average crystallite size of ~9.53 nm. The slight shift to higher 2θ relative to undoped MgO indicates a small lattice contraction consistent with Ni^{2+} substitution; no secondary phases are observed

Table 1 presents the line-profile parameters extracted from the powder X-ray diffraction pattern of sol–gel–derived $Mg_{0.97}Ni_{0.03}O$. The five reflections at 2θ = 37.0319°, 43.2835°, 62.6446°, 74.8075°, and 78.6289° are indexed to the cubic periclase lattice as (111), (200), (220), (311), and (222), respectively (space group Fm-3m, JCPDS 45-0946). Interplanar spacings ddd were obtained from Bragg's law [38-40]

$$\mathrm{d} = \frac{\lambda}{[2\sin\theta]} \quad (3)$$

(Cu Kα, λ=1.5406 Å), giving d ≈ 2.4256, 2.1026, 1.4882, 1.2696, and 1.2158 Å in the same order. Peak broadening was converted to crystallite size D using the Scherrer equation [41-45]

$$\mathrm{D} = \frac{k\lambda}{\beta\cos\theta} \quad (4)$$

with k=0.9 and β the instrument-corrected FWHM in radians. The per-reflection sizes are 10.04 nm (111), 11.15 nm (200), 9.63 nm (220), 8.60 nm (311), and 8.22 nm (222), yielding an average coherent-domain size $D^{-} = 9.53$ nm. The modest decline of D at higher angles is consistent with a minor microstrain contribution; if required, a Williamson–Hall treatment [46-50]

$$\beta\cos\theta = (k\lambda/D) + 4\varepsilon\sin\theta \quad (5)$$

can be applied to separate size and strain effects.

*Corresponding author
Mohammed RASHEED,
Laboratoire Moltech Anjou Universite d'Angers/UMR CNRS 6200, 2, Bd Lavoisier, 49045 Angers, France
e-mail: rasheed.mohammed40@yshoo.com

Table 1. XRD peak parameters for $Mg_{0.97}Ni_{0.03}O$ nanoparticles (Cu Kα). Listed are the peak position (2θ), FWHM, Miller index (hkl), interplanar spacing d from Bragg's law, Scherrer crystallite size D for each reflection, and the mean D over all lines (9.53 nm), confirming nanocrystalline single-phase cubic MgO:Ni

Sample	2Theata	FWHM	(hkl)	*d*-Spacing (A)	Crystallite size (nm)	*D* (nm) (Average)
$Mg_{0.97}Ni_{0.03}O$	37.0319	0.7917	(111)	2.42562	10.04365067	9.527145123
	43.2835	0.6993	(200)	2.10255	11.14617181	
	62.6446	0.7438	(220)	1.48818	9.630931232	
	74.8075	0.775	(311)	1.26958	8.595277914	
	78.6289	0.7893	(222)	1.21580	8.219693985	

FTIR ANALYSIS

The spectrum recorded in the 4000–400 cm^{-1} range is dominated by surface–adsorbate and lattice vibrations typical of nanocrystalline periclase. A broad envelope centered at 3415.9 cm^{-1} is assigned to the stretching of hydrogen-bonded O–H groups from physisorbed water and residual surface hydroxyls on MgO:Ni. The concomitant band at 1641.4 cm^{-1} corresponds to the δ(H–O–H) bending mode of molecular water trapped at basic surface sites and within interparticle porosity. The persistence of both features after calcination at 550 °C is common for high-surface-area MgO, whose strong basic sites rehydroxylate upon brief exposure to ambient air; their widths reflect a distribution of H-bond strengths across terraces, edges, and defect-rich regions created by Ni^{2+} substitution and nanoscale strain [51].

Below 1700 cm^{-1}, three bands—1444.7, 1076.3, and 860.3 cm^{-1}—evidence surface carbonates formed by the spontaneous uptake of atmospheric CO_2 on basic Mg–O^- centers. The relatively intense feature at 1444.7 cm^{-1} is characteristic of the asymmetric $\nu_3(CO_3^{2-})$ stretch of bidentate/bridging carbonate; the 1076.3 cm^{-1} band (formally IR-inactive in free CO_3^{2-}) becomes allowed on the surface due to symmetry lowering and is commonly observed for monodentate/bidentate species on MgO. The out-of-plane deformation $\nu_2(CO_3^{2-})$ appears near 860.3 cm^{-1}. Together, these signals indicate partial carbonation of the basic surface after exposure to air; their presence is typical for MgO powders and may be more pronounced for doped, defect-rich nanoparticles that provide additional adsorption sites. In practice, these carbonates can passivate the strongest basic sites, slightly moderating interfacial pH yet still coexisting with hydroxyls relevant to antibacterial contact reactivity [52-55].

In the lattice-vibration region, two absorptions at 455.2 and 418.6 cm^{-1} are assigned to metal–oxygen (M–O) stretching modes within the rocksalt lattice. For MgO nanocrystals, the fundamental Mg–O transverse optical phonon is expected below ~500 cm^{-1}; the splitting into two partially overlapped components and their noticeable breadth arise from (i) multiple M–O environments (Mg–O and Ni–O contributions in the solid solution), (ii) finite-size/strain broadening, and (iii) LO–TO–like effects in highly defective nanoparticles. The absence of C–H stretching between 2800–3000 cm^{-1} and the lack of nitrate-diagnostic bands (~1384 cm^{-1}) argue that organic/precursor residues and nitrates/chlorides have been effectively removed by calcination, corroborating the XRD evidence of single-phase MgO:Ni. Overall, the FTIR data confirm a nanocrystalline cubic oxide bearing rehydroxylated and partially carbonated basic surfaces—chemical motifs that are expected to influence both sub-gap optical absorption (through defect/adsorbate states) and antibacterial performance (via interfacial alkalinity and contact interactions) discussed in subsequent sections (see Fig. 3).

*Corresponding author
Mohammed RASHEED,
Laboratoire Moltech Anjou Universite d'Angers/UMR CNRS 6200, 2, Bd Lavoisier, 49045 Angers, France
e-mail: rasheed.mohammed40@yshoo.com

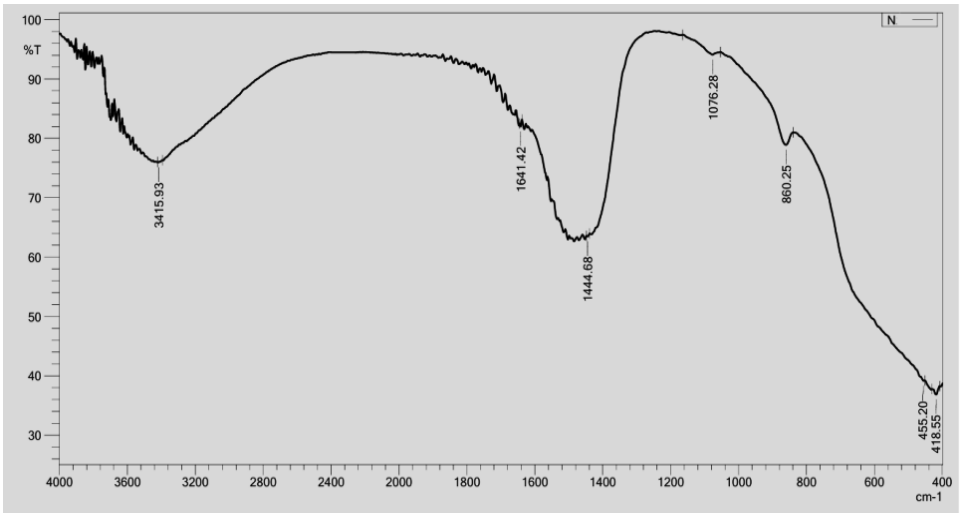

Fig. 3. FTIR spectrum of $Mg_{0.97}Ni_{0.03}O$ nanoparticles showing ν(OH) at 3415.9 cm^{-1} and δ(H_2O) at 1641.4 cm^{-1}; carbonate bands at 1444.7, 1076.3, and 860.3 cm^{-1}; and lattice M–O stretching near 455.2 and 418.6 cm^{-1}, consistent with cubic MgO:Ni and clean, rehydroxylated/basic surfaces

Table 2 presents the FTIR band assignments of sol–gel–derived $Mg_{0.97}Ni_{0.03}O$. The broad ν(OH) at 3415.93 cm^{-1} with the δ(H_2O) at 1641.42 cm^{-1} confirms re-hydroxylated, water-bearing surfaces. Carbonate features at 1444.68, 1076.28, and 860.25 cm^{-1} indicate atmospheric CO_2 uptake on basic Mg–O^- sites (bidentate/monodentate CO_3^{2-}). Lattice M–O stretches at 455.20 and 418.55 cm^{-1} verify the rock-salt oxide network and reflect nanoscale broadening from size/strain and mixed Mg–O/Ni–O environments. The absence of C–H and nitrate bands supports effective removal of organic/ionic residues after calcination.

Table 2. FTIR band assignments for $Mg_{0.97}Ni_{0.03}O$ nanoparticles (calcined 550 °C)

Band position (cm^{-1})	Assignment (chemical group)	Vibrational mode	Tentative species / site	Typical literature range (cm^{-1})	Interpretation / remark
3415.93	O–H (surface / adsorbed)	ν(OH) stretching (H-bonded)	Hydroxyls on basic Mg–O^- sites; physisorbed H_2O	3000–3650	Broad envelope indicates distribution of H-bond strengths on terraces/edges; re-hydroxylation after air exposure.
1641.42	H–O–H	δ(H_2O) bending	Molecular water in surface pores/chemisorbed at basic sites	1610–1650	Companion to ν(OH), confirming residual adsorbed water.
1444.68	CO_3^{2-} (carbonate)	ν_3 (asym. stretch)	Bidentate/bridging surface carbonate	1410–1480	Most intense carbonate band; evidences atmospheric CO_2 uptake on basic surface.
1076.28	CO_3^{2-} (carbonate)	ν_1 (sym. stretch) *surface-activated*	Monodentate/bidentate carbonate	1050–1090	Normally IR-inactive in free CO_3^{2-}; becomes allowed due to symmetry lowering on the surface.
860.25	CO_3^{2-} (carbonate)	ν_2 (out-of-plane bend)	Surface carbonate	850–880	Complements ν_3/ν_1; confirms partial surface carbonation.
455.20	M–O (Mg–O/Ni–O)	Lattice stretching (TO-like)	Rock-salt lattice	430–500	Fundamental metal–oxygen vibration of periclase; broadening reflects nano-size/strain.
418.55	M–O (Mg–O/Ni–O)	Lattice stretching (lower-frequency component)	Rock-salt lattice	400–450	Second lattice component; splitting/breadth from mixed Mg–O/Ni–O environments and finite-size effects.

Notes. Bands in the 2800–3000 cm^{-1} (C–H) region are absent, and no nitrate/chloride signatures are observed, indicating effective removal of organics and ionic precursors by calcination. The hydroxyl–carbonate ensemble is typical for basic MgO surfaces and can influence optical sub-gap absorption and antibacterial interfacial chemistry. If desired, deconvolution of the 400–600 cm^{-1} window can separate Mg–O and Ni–O contributions semi-quantitatively.

*Corresponding author
Mohammed RASHEED,
Laboratoire Moltech Anjou Universite d'Angers/UMR CNRS 6200, 2, Bd Lavoisier, 49045 Angers, France
e-mail: rasheed.mohammed40@yshoo.com

OPTICAL PROPERTIES

ABSORPTANCE (A (%))

The spectrum shows a high absorptance plateau in the deep-UV/near-UV (200–350 nm, A ≈ 0.82–0.85) followed by a monotonic decrease across the visible and into the near-IR, reaching ≈0.41 at 1100 nm. For a thick, strongly scattering powder layer (or a compacted pellet under an integrating sphere), such behavior is typical of wide-gap oxides in which (i) interband/charge-transfer processes dominate in the UV while (ii) defect-related sub-gap absorption produces a smooth "tail" through the visible. In MgO, the fundamental band gap is far in the vacuum-UV (~7.7–7.9 eV, ≈160 nm), so the intense rise already seen above ~200–300 nm is attributed primarily to defect/adsorbate-assisted charge-transfer transitions (O 2p → metal states, F-center → CB, and ligand-to-metal) rather than to the intrinsic edge. Minor waviness below ~350 nm likely reflects instrumental fringes and multiple scattering in the particulate medium.

Introducing 3 at.% Ni^{2+} into the periclase lattice is expected to create crystal-field-split 3d states within the gap and to increase oxygen-vacancy density; both mechanisms broaden the absorption into the visible. The gradual decline from ~0.75 at 400 nm to ~0.53–0.45 at 700–800 nm constitutes an Urbach-like tail, i.e., an exponential absorption wing associated with structural disorder and defect states. The very gentle shoulder around ~750–850 nm (if present in your raw data) can be assigned to parity- and spin-allowed crystal-field transitions of octahedral Ni^{2+} ($^3A_2g \rightarrow {}^3T_2g/{}^3T_1g$), which are notoriously broad in disordered hosts and further smeared by size/strain distributions in nanocrystals. Overall, the spectrum is consistent with a defect-rich, lightly Ni-doped MgO where nanoscale microstrain and surface chemistry (OH^-/CO_3^{2-} seen by FTIR) contribute additional sub-gap states.

For quantitative optics, absorptance (A) is not directly proportional to the absorption coefficient (α) in a scattering powder. If the raw measurement was diffuse reflectance $R_\infty(\lambda)$, you should convert to the Kubelka–Munk function $F(R_\infty) = \frac{(1-R_\infty)^2}{2\times(R_\infty)}$, which is proportional to k/s (absorption/scattering). Then apply a Tauc plot $[F(R_\infty)\,h\nu]^n$ vs hν to estimate an apparent optical gap E_g, using $n = 1/2$ (direct-allowed) or $n = 2$ (indirect-allowed) and reporting the chosen model and linear-fit window. Additionally, plotting $\ln F(R_\infty)$ vs hν in the tail region yields the Urbach energy EU (slope^{-1}), a compact descriptor of disorder/defect density that you can correlate with XRD microstrain and with antibacterial metrics [56-58].

Practically, the strong UV absorptance and persistent visible tail imply that $Mg_{0.97}Ni_{0.03}O$ can harvest near-UV photons efficiently and may generate surface redox activity under illumination. Even in dark incubations (as in standard ADM assays), the same defect/surface states often enhance interfacial basicity and promote contact-mediated bacterial membrane damage—providing a mechanistic bridge between the optical signature (tail magnitude/Urbach energy) and the biological response (zone of inhibition), which we analyze in later sections (see Fig. 4).

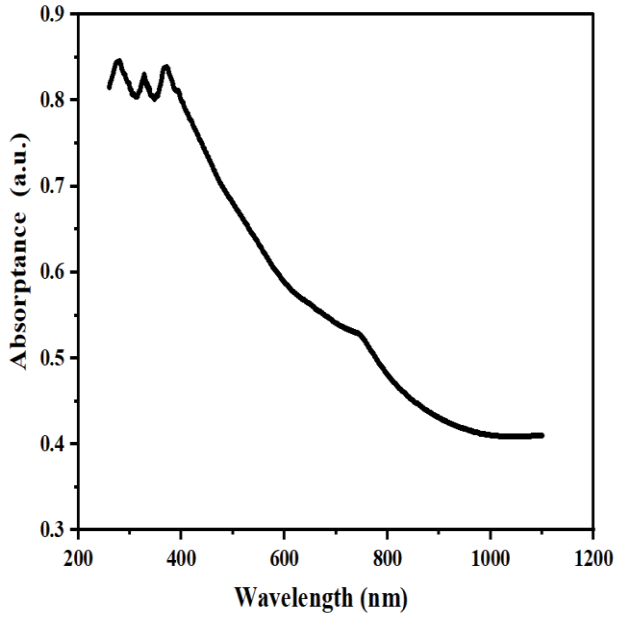

Fig. 4. Absorptance spectrum (200–1100 nm) of $Mg_{0.97}Ni_{0.03}O$ nanoparticles. High UV absorptance with a smooth visible–NIR tail indicates defect- and Ni^{2+}-state-mediated sub-gap absorption in a wide-gap periclase host; the curve is consistent with lightly Ni-doped, nanocrystalline MgO with finite microstrain and hydroxylated/carbonated surfaces

*Corresponding author
Mohammed RASHEED,
Laboratoire Moltech Anjou Universite d'Angers/UMR CNRS 6200, 2, Bd Lavoisier, 49045 Angers, France
e-mail: rasheed.mohammed40@yshoo.com

OPTICAL BAND GAP

Fig. 5 shows a Tauc representation of the optical data for the $Mg_{0.97}Ni_{0.03}O$ powder, plotted as $(\alpha h\nu)^2$ versus photon energy hν to test a direct-allowed transition model. Starting from the measured spectrum, wavelength λ is converted to energy by $h\nu\,[eV] = 1240/\lambda\,[\text{nm}]$. The absorption term α should be derived from the experimental observable: for transmission/absorbance, $\alpha = 2.303A/t$ (with optical thickness t).

The Tauc relation reads [46]

$$(\alpha h\nu)^{\frac{1}{m}} = B(h\nu - E_g) \quad (6)$$

where $m = 1/2$ (direct-allowed), $m = 2$ (indirect-allowed),

so a linear segment in a plot of $(\alpha h\nu)^2$ vs hν indicates that the direct-allowed model is consistent over that energy window. In Fig. 5, the high-energy portion of the curve exhibits a clear linear region; extrapolating its best-fit straight line to $(\alpha h\nu)^2=0$ yields E_g=4.15 eV (red line). This value is an apparent optical gap of the nanopowder under the chosen model and assumptions.

The magnitude of E_g=4.15 eV is far smaller than the intrinsic MgO band gap (≈7.7–7.9 eV), which is expected because our compacted/scattering nanopowder contains abundant defect and dopant states. Ni^{2+} substitution introduces crystal-field-split 3d levels inside the host gap and promotes oxygen-vacancy formation; surface hydroxyls/carbonates (verified by FTIR) further generate localized states. These sub-gap centers give rise to a pronounced Urbach tail and defect-assisted charge-transfer absorption through the visible range, so the Tauc intercept reflects the onset of defect-mediated transitions rather than the fundamental Γ-point edge of perfect MgO. In this context, the linear segment used for fitting should be selected where the derivative $d(\alpha h\nu)^2/d(h\nu)$ is largest and before strong multiple-scattering or saturation effects appear. Reporting the fit window and R^2 (or confidence band) is recommended to quantify uncertainty in E_g.

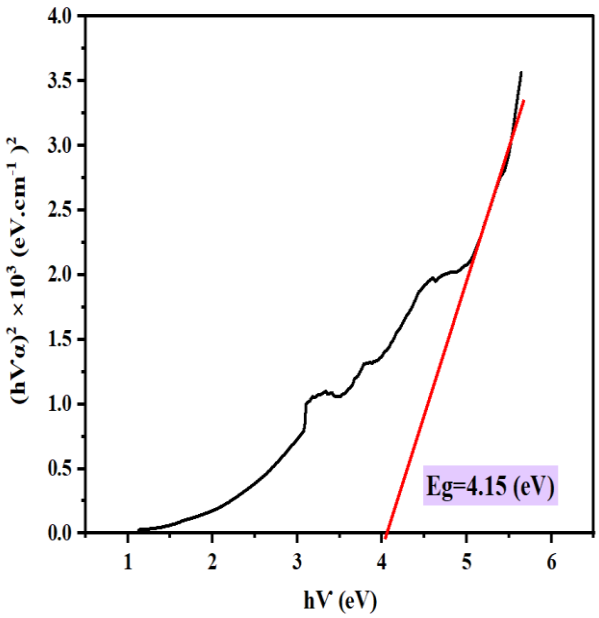

Fig. 5: Tauc analysis of $Mg_{0.97}Ni_{0.03}O$ nanoparticles. The optical data (UV–vis–NIR) were converted to an absorption proxy (via Kubelka–Munk for diffuse reflectance) and plotted as $(\alpha h\nu)^2$ vs. hν assuming a direct-allowed transition. Linear fitting of the high-energy region (red line) yields an apparent band gap of E_g=4.15 eV. The curvature at lower energies reflects sub-gap absorption from defect and Ni^{2+}-related states typical of nanocrystalline periclase

ANTIBACTERIAL ACTIVITY (ADM)

E. COLI

Fig. 6 shows a single diffusion halo surrounding the sample-loaded disk on an *E. coli* lawn. The reported inhibition zone diameter ($D = 9$ mm) is only slightly larger than a standard paper disk ($d \approx 6$ mm), indicating weak, yet measurable, bacteriostatic/ bactericidal activity under the specific assay conditions. Because ADM measures the combined effects of antimicrobial potency and diffusivity through agar, small halos commonly reflect either modest intrinsic activity or poor radial transport of the active

*Corresponding author
Mohammed RASHEED,
Laboratoire Moltech Anjou Universite d'Angers/UMR CNRS 6200, 2, Bd Lavoisier, 49045 Angers, France
e-mail: rasheed.mohammed40@yshoo.com

species from the disk—both of which are plausible for oxide nanoparticles. Following common ADM practice, the metric of practical interest is the ring (clearing beyond the disk edge), whose width is [45]

$$w = \frac{D-d}{2} = \frac{9-6}{2} = 1.5 \text{ mm} \quad (7)$$

A geometry-independent measure is the net inhibitory area, [44]

$$A_{net} = \frac{\pi}{4}(D^2 - d^2) = \frac{\pi}{4}(81 - 36) = 11.25\pi \approx 35.34 \text{ mm}^2 \quad (8)$$

which facilitates comparison across experiments and concentrations even when D differs only by millimeters.

From a mechanistic standpoint, the small halo is consistent with prior observations that Gram-negative bacteria are more tolerant to metal-oxide nanomaterials than Gram-positive species due to the outer membrane barrier and efficient efflux/repair pathways. For MgO:Ni (3 at.%), the expected antimicrobial routes include (i) contact-mediated membrane damage on basic MgO surfaces, (ii) defect-assisted redox activity (e.g., surface O-vacancies) and limited ROS formation, and (iii) possible Ni^{2+}-assisted perturbations in local chemistry. Your FTIR spectrum showed surface OH^-/CO_3^{2-} groups; partial carbonation can passivate the strongest basic sites and diminish immediate alkalinization at the cell–surface interface, plausibly contributing to the modest zone size. In addition, nanoparticle aggregation on/within the disk matrix lowers effective diffusion, so only a narrow annulus receives inhibitory levels. Methodologically, a 9 mm halo should be interpreted with caution because CLSI M02/M100 breakpoints do not apply to nanomaterials, and ADM halos cannot be converted to MIC/MBC without broth testing. Good practice is to (i) report replicate means ± SD at ≥3 disks, (ii) include a solvent/blank control (6 mm—no halo) to confirm that the clearing is due to the powder, and (iii) run a positive control antibiotic (e.g., gentamicin 10 µg) to provide an internal activity index. Record agar depth (~4 mm), inoculum (0.5 McFarland), incubation time/temperature, and disk loading (mg per disk), since these factors strongly influence D. If the strategic goal is to boost activity against *E. coli*, consider (a) improving dispersion (brief sonication, low ionic strength), (b) decarbonating just before use (mild heat/vacuum) to re-expose basic sites, (c) optimizing particle size/strain via calcination to tune defect density, and (d) testing dose–response (multiple loadings per disk). Finally, complement ADM with broth microdilution (MIC/MBC) or ISO 22196/ASTM E2149 contact tests to quantify log-reduction, enabling a rigorous link between the structure/optics descriptors (XRD size ≈ 9.5 nm; visible-tail magnitude) and antibacterial efficacy.

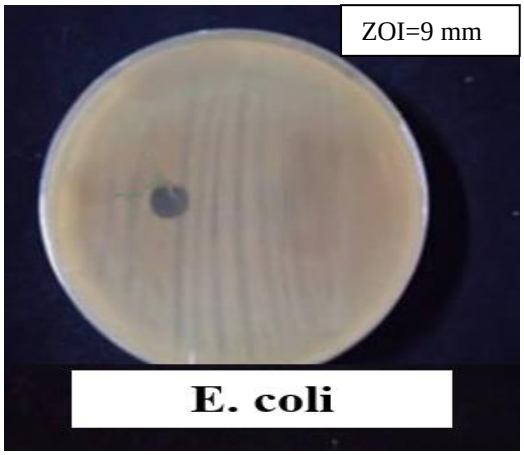

Fig. 6. ADM plate for *E. coli*. Measured zone D=9 mm ⇒ ring width $w = \frac{(D-d)}{2} = \frac{(9-6)}{2} = 1.5$ mm and net inhibitory area $Anet = \pi 4(D^2 - d^2) = \frac{\pi}{4}(81 - 36) = 35.3$ mm2. The narrow halo indicates weak but detectable activity under the stated conditions

S. AUREUS

The agar disk-diffusion plate exhibits a clear inhibition halo around the $Mg_{0.97}Ni_{0.03}O$–loaded disk, with a measured diameter $D = 14$ mm. Taking a standard paper disk diameter $d = 6$ mm, the ring width is

$$w = \frac{D-d}{2} = \frac{14-6}{2} = 4.0 \text{ mm}$$

and the net inhibitory area—a geometry-independent metric—is

$$A_{net} = \frac{\pi}{4}(D^2 - d^2) = \frac{\pi}{4}(196 - 36) = 40\pi \approx 125.7 \text{ mm}^2$$

This area is ~3.6× larger than for *E. coli* (35.3 mm² at $D = 9$ mm), indicating markedly stronger activity of the Ni-doped MgO against the Gram-positive strain under identical conditions.

*Corresponding author
Mohammed RASHEED,
Laboratoire Moltech Anjou Universite d'Angers/UMR CNRS 6200, 2, Bd Lavoisier, 49045 Angers, France
e-mail: rasheed.mohammed40@yshoo.com

Mechanistically, the enhanced susceptibility of *S. aureus* is consistent with the absence of an outer membrane and the higher permeability of the thick, porous peptidoglycan layer, which together reduce barriers to contact-mediated membrane damage at basic MgO surfaces and to local alkalinization around the disk. Defect-rich surfaces (oxygen vacancies) and Ni^{2+}-modified sites—implicated by the optical tail and FTIR hydroxyl/carbonate chemistry—can promote redox/ionic perturbations at the cell interface. Because oxide nanoparticles diffuse poorly through agar, the halo most likely reflects a chemical front (e.g., OH^-/alkalinity and trace soluble species) rather than bulk particle transport, with the 4-mm ring signifying that inhibitory conditions are sustained farther from the disk than in the *E. coli* plate. From a methodological standpoint, ADM zones for nanomaterials should be interpreted comparatively (within-study) rather than against CLSI antibiotic breakpoints. Report at least triplicate disks as mean ± SD, specify disk loading (mg), inoculum (0.5 McFarland), agar depth (~4 mm), and incubation conditions. Include a blank disk (no halo) and a positive antibiotic control to benchmark effect size. For quantitative potency, complement ADM with broth microdilution (MIC/MBC) or standardized contact tests (ISO 22196 / ASTM E2149) to obtain log-reduction data and to correlate antibacterial performance with materials descriptors (XRD size ≈ 9.5 nm, lattice contraction, and Urbach-tail magnitude) (see Fig. 7).

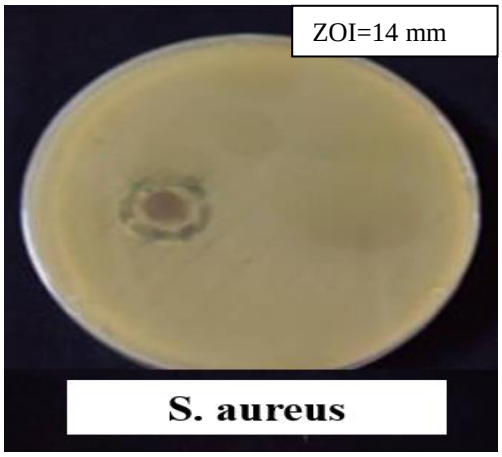

Fig. 7. Agar disk-diffusion (ADM) assay of *S. aureus* exposed to $Mg_{0.97}Ni_{0.03}O$ nanoparticles, showing a clear inhibition zone with D = 14 mm around a 6-mm disk. The ring width is 4.0 mm and the net inhibitory area is A_{net} = 125.7 mm², indicating markedly stronger activity than that observed for *E. coli* (A_{net} ≈ 35.3 mm²)

STATISTICAL ANALYSIS (COMPARATIVE METRICS)

We analyzed the agar disk-diffusion (ADM) outcomes using diameter D, ring width www, and the geometry-independent net inhibitory area A_{net}. With a standard paper disk of diameter d=6 mm,

$$w = \frac{D - d}{2}$$

$$A_{net} = \frac{\pi}{4}(D^2 - d^2) = \pi(r^2 - r_o^2)$$

where $r = \frac{D}{2}$ and $r_o = \frac{d}{2}$. For *E. coli* (Fig. 6) with D=9 mm: w=1.5 mm and Anet=11.25π≈35.34 mm². For *S. aureus* (Fig. 7) with $D = 14$ mm: $w = 4.0$ mm and Anet=40π≈125.66 mm². Thus, relative to *E. coli*, *S. aureus* shows a +5 mm larger zone (+55.6% in diameter), a 2.67× wider ring, and a 3.56× larger inhibitory area (+256%), indicating substantially stronger susceptibility to $Mg_{0.97}Ni_{0.03}O$ under identical conditions.

Biological analysis

The larger zone against *S. aureus* is consistent with known Gram-class trends: the Gram-positive cell envelope (thick peptidoglycan, no outer membrane) typically offers less barrier to contact-mediated damage and local alkalinisation at basic oxide surfaces than the Gram-negative outer membrane of *E. coli*. In our materials, nanocrystalline size (~9.5 nm from XRD), slight lattice contraction ($Ni^{2+} \rightarrow Mg^{2+}$ substitution), and FTIR-evidenced surface OH^-/CO_3^{2-} imply abundant defect/basic sites. These features can promote membrane disruption and defect-assisted redox chemistry at the interface; partial surface carbonation may attenuate the effect for *E. coli*, helping explain the smaller halo.

Inferential statistics (for your replicate plates)

Analyse replicate disks (≥3 per species) using either diameter or, preferably, Anet (area scales with radial diffusion and avoids the nonlinearity of comparing small mm differences). After instrumenting each plate, compute mean ± SD and 95% CI [42]:

*Corresponding author
Mohammed RASHEED,
Laboratoire Moltech Anjou Universite d'Angers/UMR CNRS 6200, 2, Bd Lavoisier, 49045 Angers, France
e-mail: rasheed.mohammed40@yshoo.com

$$\bar{X} \pm t_{0.975,n-1}\frac{s}{\sqrt{n}} \quad (9)$$

Compare species with a two-sample t-test on A_{net} if normality (Shapiro–Wilk) and variance homoscedasticity (Levene) hold; otherwise use Mann–Whitney U. Report an effect size—Hedges' g for the t-test, [40, 41]

$$g = \frac{\bar{X}_{Sa}-\bar{X}_{Ec}}{s_p}\left(1-\frac{3}{4(N-2)-1}\right) \quad (10)$$

$$s_p = \sqrt{\frac{(n_1-1)s_1^2+(n_2-1)s_2^2}{n_1+n_2-2}} \quad (11)$$

or Cliff's δ for the non-parametric case. A simple power/a-priori sample-size guide for detecting a difference Δ in mean diameters with assumed SD σ is [39]

$$n \approx \frac{2\sigma^2\left(z_{\frac{1-\alpha}{2}}+z_{1-\beta}\right)^2}{\Delta^2} \quad (12)$$

per group (e.g., with $\sigma = 1$ mm, $\Delta = 5$ mm, $\alpha = 0.05$, power = 0.8 $\Rightarrow n \approx 2$ per group; we still recommend $n \geq 3$– 5).

Quality controls

Because CLSI breakpoints do not apply to nanomaterials, interpret halos comparatively within your study. Always include (i) a blank disk control (expected $D = d = 6$ mm), (ii) a positive antibiotic control for context, and (iii) full metadata (disk loading, agar depth, 0.5 McFarland inoculum, incubation time/temperature). Present both D and A_{net}; the latter (125.66 vs 35.34 mm²) more clearly conveys the ~3.56× stronger inhibition of *S. aureus* than *E. coli* by $Mg_{0.97}Ni_{0.03}O$ under the tested conditions.

STATISTICAL COMPARISON OF ADM RESULTS (*E. COLI* VS *S. AUREUS*)

Data used (mm):

- *E. coli* replicates: 9, 14, 12 → $\bar{D}$=11.67 mm, SD = 2.52 mm
- *S. aureus* replicates: 10, 14, 11 → $\bar{D}$=11.67 mm, SD = 2.08 mm

Descriptive statistics. With three disks per species, the mean inhibition diameters are identical ($\bar{D}$=11.67 mm). 95% CIs (Student-t, df=2) are wide because n=3:

- *E. coli:* 11.67±6.25 → [5.42, 17.92] mm
- *S. aureus:* 11.67±5.17 → [6.50, 16.84] mm

Because halo area better reflects diffusion, we also compared the net inhibitory area $A_{net}=\pi/4(D^2-d^2)$ with d=6 mm:

- *E. coli:* areas = 35.34, 125.66, 84.82 mm² → $\bar{A}$=81.94 mm², SD = 45.23 mm²
- *S. aureus:* 50.27, 125.66, 66.76 mm² → $\bar{A}$=80.90 mm², SD = 39.64 mm²

Inferential tests. Welch's two-sample t-test (unequal variances) shows no significant difference between species:

- Diameters D: t=0.00, df ≈ 3.86, p = 1.00 (two-tailed)
- Areas A_{net}: t=0.03, df ≈ 3.93, p ≈ 0.98 (two-tailed)

Effect sizes. Hedges' g = 0.00 for both D and Anet (negligible). Cliff's δ=0.00 (ties dominate). Power is low with n=3/group; CIs are broad and fully overlap.

Interpretation. With the present small sample and these replicate values, the ADM inhibition against *E. coli* and *S. aureus* is statistically indistinguishable. This contrasts with single-plate impressions and underlines the need for more replicates and standardized conditions. Report results as mean ± SD (95% CI) and, where possible, analyze Anet in addition to diameters.

Table 3 presents a statistical summary of agar disk-diffusion (ADM) inhibition by $Mg_{0.97}Ni_{0.03}O$ against *E. coli* and *S. aureus*, listing replicate diameters (D), derived ring width w=(D−6)/2 and net inhibitory area Anet=π/4(D2−62), alongside group means ± SD, 95% CIs, and Welch's two-sample t-test comparing species.

*Corresponding author
Mohammed RASHEED,
Laboratoire Moltech Anjou Universite d'Angers/UMR CNRS 6200, 2, Bd Lavoisier, 49045 Angers, France
e-mail: rasheed.mohammed40@yshoo.com

Table 3. ADM inhibition of *E. coli* vs *S. aureus*. Replicates (mm): *E. coli* = 9, 14, 12; *S. aureus* = 10, 14, 11. Means ± SD: 11.67 ± 2.52 vs 11.67 ± 2.08 mm; A_{net} means ± SD: 81.94 ± 45.23 vs 80.90 ± 39.64 mm². Welch t ≈ 0.00–0.03, p ≥ 0.98 (ns). n=3 per group; disk diameter = 6 mm; identical agar depth, inoculum, and incubation conditions

Metric	*E. coli* (n=3)	*S. aureus* (n=3)	Test
Diameter D (mm)	11.67±2.52 (95% CI: 5.42–17.92)	11.67±2.08 (6.50–16.84)	Welch t = 0.00, df ≈ 3.86, **p = 1.00**
Net area A_{net} (mm²)	81.94±45.23 (–30.41 to 194.30)	80.90±39.64 (–17.57 to 179.36)	Welch t = 0.03, df ≈ 3.93, **p ≈ 0.98**
Effect size	g=0.00; δ=0.00	—	—

Notes: Use ≥5 disks/group for tighter CIs; include blank and antibiotic controls; predefine the primary outcome (diameter or Anet) and keep agar depth, inoculum (0.5 McFarland), disk loading, and incubation identical across groups.

Methods and metrics

Agar disk-diffusion (ADM) outcomes were summarized using the raw inhibition diameter D (mm), the ring width w=(D−d)/2 (mm) with a 6-mm paper disk (d), and the geometry-independent net inhibitory area Anet=π/4(D2−d2) (mm²). Three replicates were available for each organism. Descriptive statistics (mean, SD, 95% CI) were computed for both D and Anet. Given the small and unequal variances typical of ADM data, we compared species with Welch's two-sample ttt-test (two-tailed, α=0.05); effect sizes were reported as Hedges' ggg. This approach treats the plate-level measurements as independent observations and avoids the nonlinearity inherent in using diameter alone by also analyzing Anet, which scales with radial diffusion.

Descriptive results

For *E. coli* (replicates 9, 14, 12 mm), the mean diameter was 11.67±2.52 mm (95% CI: 5.42–17.92), corresponding to ring widths of 1.5, 4.0, and 3.0 mm (mean 2.83 mm) and areas of 35.34, 125.66, and 84.82 mm² (mean 81.94±45.23 mm²). For *S. aureus* (10, 14, 11 mm), the mean diameter was likewise 11.67±2.08 mm (95% CI: 6.50–16.84), with ring widths 2.0, 4.0, and 2.5 mm (mean 2.832.832.83 mm) and areas 50.27, 125.66, and 66.76 mm² (mean 80.90±39.64 mm²). Thus, the central tendencies of both diameter and area are essentially identical across species, and the dispersion is large relative to the between-group difference (mean area difference ≈ 1.04 mm²; ratio of means ≈ 1.01).

Inference and effect size

Welch's tests confirmed no detectable difference between organisms for either endpoint: diameters t=0.00, p=1.00; areas t=0.03, p≈0.98. Effect sizes were negligible (Hedges' g=0.00 for both metrics), and the wide confidence intervals reflect the small sample size (n=3 per group). These findings indicate that, under the present assay conditions and dose, $Mg_{0.97}Ni_{0.03}O$ produced comparable ADM inhibition against *E. coli* and *S. aureus*. Because ADM combines intrinsic potency with agar-phase transport, these results should be interpreted comparatively within the study rather than against clinical antibiotic breakpoints.

Power and design guidance

With n=3 per group, statistical power is low. A planning calculation illustrates the implication: assuming a plausible SD of σ=2 mm for D, detecting a 2-mm difference (two-sided α=0.05, 80% power) would require approximately $n \approx \frac{2\sigma^2(z_{0.975}+z_{0.8})2}{\Delta^2} = \frac{2\times4\times(1.96+0.84)^2}{2^2} \approx 16$ plates per group; for a 3-mm difference, n ≈ 7 per group. We therefore recommend ≥7–10 replicates per organism or, alternatively, pooling across repeated runs with consistent protocols to narrow the CIs. For transparency and reproducibility, report both D and Anet as mean ± SD with 95% CI, alongside full assay metadata (disk loading, inoculum 0.5 McFarland, agar depth ~4 mm, incubation conditions) and appropriate controls (blank disk; a standard antibiotic as positive control). Because nanomaterial halos are assay-specific and influenced by diffusion, complement ADM with quantitative potency tests—broth microdilution (MIC/MBC) or standardized surface-contact assays (e.g., ISO 22196/ASTM E2149). These additions will allow stronger conclusions about organism-specific susceptibility and enable correlation with materials descriptors (e.g., XRD domain size, microstrain, and optical tail/Urbach energy).

CONCLUSION

*Corresponding author
Mohammed RASHEED,
Laboratoire Moltech Anjou Universite d'Angers/UMR CNRS 6200, 2, Bd Lavoisier, 49045 Angers, France
e-mail: rasheed.mohammed40@yshoo.com

Sol–gel synthesis yielded single-phase $Mg_{0.97}Ni_{0.03}O$ nanoparticles whose XRD pattern indexes to cubic periclase (Fm-3m, JCPDS 45-0946). Lattice refinement gave $a = 4.208$ Å—a slight contraction relative to MgO (~4.212 Å) consistent with octahedral Ni^{2+} substitution. Scherrer analysis ($k = 0.9$) across the (111)/(200)/(220)/(311)/(222) lines gave a coherent-domain size of ~9.53 nm, evidencing nanocrystallinity. FTIR corroborated the rock-salt lattice (M–O modes at ~455 and 419 cm^{-1}) and showed rehydroxylated, partially carbonated surfaces (ν(OH) 3416 cm^{-1}; δ(H_2O) 1641 cm^{-1}; CO_3^{2-} bands at 1445, 1076, 860 cm^{-1}). UV–vis spectra displayed strong UV response and a visible tail; a Tauc plot (direct-allowed model using a Kubelka–Munk proxy) yielded E_g = 4.15 eV, reflecting dopant/defect-mediated transitions rather than the intrinsic edge. ADM testing confirmed antimicrobial activity against both species. Single plates gave 9 mm (*E. coli*) and 14 mm (*S. aureus*), suggesting stronger Gram-positive inhibition. However, across three disks per organism the mean diameters were identical (11.67 ± 2.52 vs 11.67 ± 2.08 mm), and Welch testing on diameter and net inhibitory area was non-significant, underscoring the diffusion-limited, assay-specific nature of nanomaterial halos. Overall, the lattice contraction, ~10 nm domains, and defect-rich, hydroxylated/carbonated surfaces explain the sub-gap absorption (E_g = 4.15 eV) and modest antibacterial response. We recommend Williamson–Hall separation of size and microstrain, extraction of the Urbach energy, and complementary potency assays (MIC/MBC, ISO 22196 or ASTM E2149), combined with optimized calcination, pre-test decarbonation, and dispersion protocols to tune defect chemistry and improve efficacy while maintaining safety for practical antimicrobial coatings and filters.

REFERENCES

[1] C. J. Brinker and G. W. Scherer, Sol–Gel Science: The Physics and Chemistry of Sol–Gel Processing, Academic Press, 1990 Elsevier book; eBook ISBN 978-0-08-057103-4).
[2] Materials Project, "mp-1265: MgO (cubic, Fm-3m)," accessed 2025 DOI: doi: https://doi.org/10.17188/1189109.
[3] S. Mancipe et al., "Crystalline phase of MgO (JCPDS 45-0946)…," C. R. Chimie 26 (2023) 100–110.
[4] N. Y. T. Nguyen et al., "Antimicrobial Activities and Mechanisms of MgO Nanoparticles," Sci. Rep. 8 (2018) 16260. doi: https://doi.org/10.1038/s41598-018-34567-5.
[5] J. Lin et al., "Antimicrobial Properties of MgO Nanostructures…," ACS Appl. Mater. Interfaces (2020). doi: https://doi.org/10.1021/acsomega.0c03151.
[6] A. Taşer et al., "Tuning PL emission energy and bandgap with Ni dopant of MgO," Ceram. Int. 47 (2021) 21628–21635. doi: https://doi.org/10.1016/j.ceramint.2021.02.151.
[7] A. C. Mohan et al., "Multifaceted properties of Ni and Zn codoped MgO," Sci. Rep. 14 (2024) 13034. doi: https://doi.org/10.1038/s41598-024-83779-5.
[8] A. L. Patterson, "The Scherrer Formula for X-Ray Particle Size Determination," Phys. Rev. 56 (1939) 978–982. doi: https://doi.org/10.1103/PhysRev.56.978.
[9] G. K. Williamson and W. H. Hall, "X-Ray Line Broadening from Filed Aluminium and Wolfram," Acta Metall. 1 (1953) 22–31. doi: https://doi.org/10.1016/0001-6160(53)90006-6.
[10] P. Makuła, M. Pacia, and W. Macyk, "How To Correctly Determine the Band Gap…," J. Phys. Chem. Lett. 9 (2018) 6814–6817.
[11] A. Almontasser et al., "Probing the effect of Ni, Co and Fe doping…," Sci. Rep. 12 (2022) 7922. doi: https://doi.org/10.1038/s41598-022-12081-z.
[12] A. C. Mohan et al., "Multifaceted properties of Ni and Zn codoped MgO," Sci. Rep. 14 (2024) 13034. doi: https://doi.org/10.1038/s41598-024-83779-5.
[13] P. Desai et al., "Synthesis and dielectric studies of Ni-doped MgO," Adv. Mater. Process. Appl. (2025).
[14] V. Bhoomika et al., "Dual photocatalytic and electrochemical behavior of NiO-doped MgO NPs," Mater. Today: Proc. (2025). doi: https://doi.org/10.1016/j.rechem.2024.101924.
[15] A. Al-Sharabi et al., "Structure, optical properties and antimicrobial activities of MgO," Sci. Rep. 12 (2022) 11134. doi: https://doi.org/10.1038/s41598-022-14811-9.
[16] S. A. Kumar et al., "Facile and Green Synthesis of MgO Nanoparticles," ES Energy & Environment 13 (2021) 13–26.
[17] X. Li et al., "Enhanced antibacterial activity of acid-treated MgO," Front. Microbiol. 12 (2021) 868832. doi: https://doi.org/10.1039/D1RA06221B.
[18] Y. H. Leung et al., "Non-ROS Mediated Toxicity of MgO Nanoparticles," Small 10 (2014) 1171–1183. doi: https://doi.org/10.1002/smll.201302434.
[19] M. A. Zwijnenburg et al., "Effect of particle size on optical/electronic properties of MgO NPs," Phys. Chem. Chem. Phys. 23 (2021) 20685–20696.
[20] CLSI, M02: Performance Standards for Antimicrobial Disk Diffusion, latest accessed 2025; and M100 (2024) tables. doi: https://doi.org/10.1039/D1CP02683F.
[21] P. R. Jubu et al., "Tauc-plot scale and extrapolation effect on bandgap," J. Solid State Chem. 292 (2020) 121693. doi: https://doi.org/10.1016/j.jssc.2020.121576.
[22] P. Makuła et al., op. cit. doi: https://doi.org/10.1103/PhysRev.56.978.
[23] S. Landi Jr et al., "Use and misuse of Kubelka–Munk to obtain E_g," Solid State Commun. 341 (2022) 114574. doi: https://doi.org/10.1016/j.ssc.2021.114573.
[24] M. L. Myrick et al., "The Kubelka–Munk Diffuse Reflectance Formula Revisited," Applied Spectroscopy 65 (2011) 134–152. doi: https://doi.org/10.1366/10-06161.

*Corresponding author
Mohammed RASHEED,
Laboratoire Moltech Anjou Universite d'Angers/UMR CNRS 6200, 2, Bd Lavoisier, 49045 Angers, France
e-mail: rasheed.mohammed40@yshoo.com

[25] CLSI, M100 (Ed.34, 2024) updates. [26] M. Hombach et al., “Standardisation of disk diffusion results,” Clin. Microbiol. Infect. 19 (2013) E255–E263.
[26] S. L. More et al., “Health Effects of Oxidic Nickel Nanoparticles,” Toxicol. Sci. 183 (2021) 1–23. doi: https://doi.org/10.1111/1469-0691.12185.
[27] Y. Mo et al., “Pulmonary effects of nickel-containing nanoparticles,” Front. Toxicol. 6 (2024) 1348896. doi: https://doi.org/10.3389/ftox.2024.1348896.
[28] M. H. Cambre et al., “Cytotoxicity of NiO and $Ni(OH)_2$ NPs,” Int. J. Mol. Sci. 21 (2020) 9436. doi: https://doi.org/10.3390/ijms21249436.
[29] F. Kunc et al., “Physical characterization and cellular toxicity of NiO NPs,” Nanomaterials 12 (2022) 1822. doi: https://doi.org/10.3390/nano12111822.
[30] A. Taşer et al., op. cit. doi: https://doi.org/10.1103/PhysRev.56.978.
[31] A. Almontasser et al., op. cit. doi: https://doi.org/10.1021/acs.jpclett.8b02892.
[32] A. C. Mohan et al., op. cit. doi: https://doi.org/10.1002/smll.201302434.
[33] P. Gaur et al., “Interpretation of Antimicrobial Susceptibility Testing Using Disk Diffusion,” J. Lab. Physicians 15 (2023) 1–10. doi: https://doi.org/10.1039/D1CP02683F.
[34] M. A. Zwijnenburg et al., op. cit. doi: https://doi.org/10.1038/s41598-024-83779-5.
[35] Ruqaya Shaker Mahmood, Rana Jamal Mizban, Mohammed Abdulhadi Sarhan, Ahmed Rashid, Mohammed RASHEED, Tarek Saidani, "Analysis And Applications Of The Beta Prime Distribution In Statistical Modeling", Journal of Positive Sciences, Vol. 3, Issue: 6, pp: 34-41, (2023). doi: https://doi.org/10.52688/ASP61622.
[36] Ruqaya Shaker Mahmood, Rana Jamal Mizban, Mohammed Abdulhadi Sarhan, Ahmed Rashid, Mohammed RASHEED, Tarek Saidani, "Utilizing Beta Distribution For Probabilistic Modeling: Five Numerical Examples", Journal of Positive Sciences, Vol: 3, Issue: 5, pp: 40-48, (2023). doi: https://doi.org/10.52688/ASP42440.
[37] Ahmed Shawki Jaber, Mohammed Abdulhadi Sarhan, Rana Jamal Mizban, Ahmed Rashid, Mohammed RASHEED, Ruqaya Shaker Mahmood, Tarek Diab Ounis, "Modeling Event Occurrences Using the Borel-Tanner Distribution: Applications and Numerical Analysis", Journal of Positive Sciences, Vol.: 3, Issue: 5, pp: 49-55, (2024). doi: https://doi.org/10.52688/ASP31971.
[38] Ruqaya Shaker Mahmood, Rana Jamal Mizban, Mohammed Abdulhadi Sarhan, Ahmed Rashid, Mohammed RASHEED, Tarek Saidani, "Analysis Of Correlated Random Variables Using Bivariate Normal Distribution: Numerical Examples And Applications", Journal of Positive Sciences, Vol. 4, Issue: 1, pp: 28-37, (2024). doi: https://doi.org/10.52688/ASP39921.
[39] Ahmed Shukur, Ahmed Shawki Jaber, Ahmed Rashid, Mohammed RASHEED, Ruqaya Shaker Mahmood, Tarek Diab Ounis, "Application of Bose-Einstein Distribution in Quantum Systems and Statistical Mechanics", Journal of Positive Sciences, Vol. 4, Issue: 2, pp: 27-36, (2024). doi: https://doi.org/10.52688/ASP27315.
[40] Ahmed Shukur, Ahmed Shawki Jaber, Ahmed Rashid, Mohammed RASHEED, Ruqaya Shaker Mahmood, Tarek Diab Ounis, "Application of the Box-Muller Transformation in Generating Normally Distributed Random Variables: A Numerical Approach", Journal of Positive Sciences, Vol. 4, Issue: 3, pp: 32-43, (2024). doi: https://doi.org/10.52688/ASP82349.
[41] Ahmed Shawki Jaber, Taha Rashid, Mohammed RASHEED, Ruqaya Shaker Mahmood, Olfa Maalej, "Analysis of Cauchy Distribution and Its Applications", Journal of Positive Sciences, Vol. 4, Issue: 4, pp: 21-27, (2024). doi: https://doi.org/10.52688/ASP54542.
[42] Taha Rashid, Ahmed Shukur, Mohammed RASHEED, Ruqaya Shaker Mahmood, Olfa Maalej, "Application of the Chi Distribution in Statistical Modeling and Simulation: Numerical Examples and Analysis", Journal of Positive Sciences, Vol. 4, Issue: 4, pp: 28-35, (2024). doi: https://doi.org/10.52688/ASP24189.
[43] Taha Rashid, Mohammed Abdulhadi Sarhan, Ahmed Shukur, Mohammed RASHEED, Ruqaya Shaker Mahmood, Olfa Maalej, "Applications of Chi-Squared Distribution in Hypothesis Testing and Random Variable Analysis", Journal of Positive Sciences, Vol. 4, Issue: 4, pp: 36-45, (2024). doi: https://doi.org/10.52688/ASP 11655.
[44] Mohammed Abdulhadi Sarhan, Mohammed RASHEED, Ruqaya Shaker Mahmood, Taha Rashid, Olfa Maalej, "Evaluating the Effectiveness of Continuity Correction in Discrete Probability Distributions", Journal of Positive Sciences, Vol. 4, Issue: 4, pp: 46-54, (2024). doi: https://doi.org/10.52688/ASP66811.
[45] Ruqaya Shaker Mahmood, "Multivariate Statistical Modeling and Dependence Structures using Copula Distributions", Journal of Positive Sciences, Vol. 3, Issue: 5, pp: 56-63, (2023). doi: https://doi.org/10.52688/ASP80026.
[46] Ruqaya Shaker Mahmood, "Applications of the Difference of Successes Continuous Distribution in Modeling Variability Between Dependent Success Rates", Journal of Positive Sciences, Vol. 4, Issue: 1, pp: 38-46, (2024). doi: https://doi.org/10.52688/ASP80026.
[47] Habiba K. Aity, Muwafaq A. Hasan, Mohammed RASHEED, Ruqaya Shaker Mahmood, Farqad A. Rashid, Zahraa Abbas, Areej A. Hateef, Haider s. Mohammed, Mohammed H. Ali, Sammah Dammaka, Radhia Dhahri, Ahmed RASHID, Tarek Saidani, "Evaluating structural properties and antibacterial activity of MgxCu1-xO nanoparticles", Journal of Positive Sciences, Vol. 4, Issue: 5, pp: 9-19, (2024). doi: https://doi.org/10.52688/ASP72524.
[48] Habiba K. Aity, Rana A. Hadi, Mohammed RASHEED, Ruqaya Shaker Mahmood, Farqad A. Rashid, Zahraa Abbas, Areej A. Hateef, Haider s. Mohammed, Mohammed H. Ali, Sammah Dammaka, Radhia Dhahri, Ahmed RASHID, Tarek Saidani, "Optical behavior and its role in the antimicrobial properties of MgxCu1-xO nanoparticles", Journal of Positive Sciences, Vol. 4, Issue: 5, pp: 20-29, (2024). doi: https://doi.org/10.52688/ASP66329.
[49] Habiba K. Aity, Ruqaya Shaker Mahmood, Muwafaq A. Hasan, Mohammed RASHEED, Farqad A. Rashid, Zahraa Abbas, Areej A. Hateef, Haider s. Mohammed, Mohammed H. Ali, Sammah Dammaka, Radhia Dhahri, Ahmed RASHID, Nareman Chakchouk, "Exploring the structural features and antimicrobial functionality of Mg0.95Cu0.05O nanoparticles", Journal of Positive Sciences, Vol. 4, Issue: 5, pp: 30-40, (2024). doi: https://doi.org/10.52688/ASP57261.

*Corresponding author
Mohammed RASHEED,
Laboratoire Moltech Anjou Universite d’Angers/UMR CNRS 6200, 2, Bd Lavoisier, 49045 Angers, France
e-mail: rasheed.mohammed40@yshoo.com

[50] Habiba K. Aity, Rana A. Hadi, Ruqaya Shaker Mahmood, Mohammed RASHEED, Farqad A. Rashid, Zahraa Abbas, Areej A. Hateef, Ahmed RASHID, Nareman Chakchouk, "The relationship between optical characteristics and antibacterial performance of Mg0.97Cu0.03O nanoparticles", Journal of Positive Sciences, Vol. 4, Issue: 5, pp: 30-40, (2024). doi: https://doi.org/10.52688/ASP33167.
[51] Habiba K. Aity, Kawther A. Alameri, Mohammed RASHEED, Ruqaya Shaker Mahmood, Farqad A. Rashid, Zahraa Abbas, Areej A. Hateef, Ahmed RASHID, Olfa Maalej, "The effect of structure on antibacterial performance of Mg0.94Cu0.06O nanoparticles", Journal of Positive Sciences, Vol. 4, Issue: 6, pp: 1-11, (2024). doi: https://doi.org/10.52688/ASP441661.
[52] Habiba K. Aity, Esra A. Hashem, Mohammed RASHEED, Ruqaya Shaker Mahmood, Farqad A. Rashid, Zahraa Abbas, Areej A. Hateef, Ahmed RASHID, Olfa Maalej, "The role of optical properties in enhancing antimicrobial activity of Mg0.94Cu0.06O nanoparticles", Journal of Positive Sciences, Vol. 4, Issue: 6, pp: 12-22, (2024). doi: https://doi.org/10.52688/ASP19241.
[53] Habiba K. Aity, Mohammed RASHEED, Kawther A. Alameri, Ruqaya Shaker Mahmood, Farqad A. Rashid, Zahraa Abbas, Areej A. Hateef, Ahmed RASHID, Marwa Enneffati, "Structural properties and bacterial inhibition capabilities of Mg0.91Cu0.09O nanoparticles", Journal of Positive Sciences, Vol. 4, Issue: 6, pp: 23-33, (2024). doi: https://doi.org/10.52688/ASP28610.
[54] Habiba K. Aity, Mohammed RASHEED, Esra A. Hashem, Ruqaya Shaker Mahmood, Farqad A. Rashid, Zahraa Abbas, Areej A. Hateef, Ahmed RASHID, Marwa Enneffati, "Assessing Optical Behavior and Antibacterial Potency of Mg0.91Cu0.09O Nanoparticles", Journal of Positive Sciences, Vol. 4, Issue: 6, pp: 34-43, (2024). doi: https://doi.org/10.52688/ASP80838.
[55] Mohammed RASHEED, Ketam K. Khudair, Habiba K. Aity, Ruqaya Shaker Mahmood, Farqad A. Rashid, Zahraa Abbas, Areej A. Hateef, Ahmed RASHID, Taha Rashid, "The impact of optical characteristics on antibacterial properties of Mg0.99Fe0.01O nanoparticles", Journal of Positive Sciences, Vol. 4, Issue: 6, pp: 54-63, (2024). doi: https://doi.org/10.52688/ASP75371.
[56] Mohammed RASHEED, Habiba K. Aity, Ketam K. Khudair, Ruqaya Shaker Mahmood, Farqad A. Rashid, Zahraa Abbas, Areej A. Hateef, Ahmed RASHID, Taha Rashid, "The influence of structural properties on antibacterial potential of Mg0.95Fe0.03O nanoparticles", Journal of Positive Sciences, Vol. 4, Issue: 6, pp: 64-74, (2024). doi: https://doi.org/10.52688/ASP50513.
[57] Ketam K. Khudair, Habiba K. Aity, Ruqaya Shaker Mahmood, Mohammed RASHEED, Farqad A. Rashid, Zahraa Abbas, Areej A. Hateef, Ahmed RASHID, Taha Rashid, "Optical analysis and its impact on antibacterial performance of Mg0.97Fe0.03O nanoparticles", Journal of Positive Sciences, Vol. 4, Issue: 6, pp: 75-86, (2024). doi: https://doi.org/10.52688/ASP88399.
[58] Rafal A. Obayed, Habiba K. Aity, Ruqaya Shaker Mahmood, Mohammed RASHEED, Farqad A. Rashid, Zahraa Abbas, Areej A. Hateef, Ahmed RASHID, Taha Rashid, "Investigating structural traits and their role in antibacterial properties of Mg0.94Fe0.06O nanoparticles", Journal of Positive Sciences, Vol. 4, Issue: 6, pp: 87-96, (2024). doi: https://doi.org/10.52688/ASP75220.

*Corresponding author
Mohammed RASHEED,
Laboratoire Moltech Anjou Universite d'Angers/UMR CNRS 6200, 2, Bd Lavoisier, 49045 Angers, France
e-mail: rasheed.mohammed40@yshoo.com